Research Square

Preprints are preliminary reports that have not undergone peer review.
They should not be considered conclusive, used to inform clinical practice,
or referenced by the media as validated information.

Newton's Constant from Horizon-Selected Quantum Capacity and Electroweak Determinant Closure

Shalender Singh

singhshalender@gmail.com

Independent Researcher

Vishnu Priya Singh Parmar

Independent Researcher

Research Article

Keywords: finite causal cell, Newton constant, Fermi constant, electroweak determinant closure, horizon entropy, relational coframe

Posted Date: August 18th, 2026

DOI: https://doi.org/10.21203/rs.3.rs-10639471/v1

License: This work is licensed under a Creative Commons Attribution 4.0 International License.
Read Full License

Additional Declarations: No competing interests reported.

Newton's Constant from Horizon-Selected Quantum Capacity and Electroweak Determinant Closure

Shalender Singh[a,*], Vishnu Priya Singh Parmar[a]

[a] *Independent researchers, Milpitas, California, USA*

Abstract

Why gravity is so weak relative to electroweak interactions remains unexplained, and Newton's constant remains an independent normalization in most microscopic models. We introduce an explicit hybrid finite causal-cell model that links the Newton and Fermi constants through a horizon-selected quantum capacity. Eight body-centered-cubic routes and a recurrence coin define a gapped occupied history; four Gauss-invariant ports reconstruct a centered-Gram coframe; Cartan transport and a relational constraint complex leave two tensor helicities. The same occupied history yields a positive tensor response and an endpoint Julia entropy. Generalized horizon entropy selects the integer capacity $K_* = 362$, with occupied rank $D_* = 107\,232\,946\,821$. Complete lower-branch occupation and the oriented three-slot coframe volume produce the exact reduction D_*^{-3}. The remaining normalization is specified by an electroweak determinant closure on the doubled six-component coframe shell: multiplicativity selects the determinant as the scalar transfer character, while least logarithmic history yields the twelfth root of $\mathcal{R}_{\mathrm{EW}} = \sqrt{2}G_F M_W^2(1 - M_W^2/M_Z^2)/[\pi\alpha(0)]$. The resulting sum rule, $G_{\mathrm{pred}} = G_F\mathcal{R}_{\mathrm{EW}}^{1/12}/(\sqrt{2}D_{362}^3)$, gives $6.67484(28) \times 10^{-11}\,\mathrm{m^3\,kg^{-1}\,s^{-2}}$ from current non-gravitational inputs, 1.72 combined standard deviations from the CODATA value. The relation joins horizon entropy, finite quantum geometry, and precision electroweak data in one quantitative test, with improved W-mass measurements, complete horizon-edge accounting, and coframe-shell isotropy providing independent experimental and structural checks.

Keywords: finite causal cell, Newton constant, Fermi constant, electroweak

*Corresponding author

Email address: singhshalender@gmail.com (Shalender Singh)

determinant closure, horizon entropy, relational coframe

1. Introduction

Newton's constant sets the scale at which energy-momentum curves spacetime, yet it enters general relativity as an independent normalization. This remains true in most microscopic approaches: a model may produce a massless spin-two mode or an Einstein-like continuum action while leaving the coefficient of that action, the microscopic event scale, or the ultraviolet representation sector unspecified. A derivation of the observed gravitational strength therefore requires more than a healthy graviton. It must connect the spin-two normalization to non-gravitational observables and remove the discrete sector freedom without using measured gravity in either step.

Two established lines of thought motivate such a connection. Induced-gravity calculations relate the Einstein coefficient to quantum response [1, 3, 10], while horizon thermodynamics and entanglement relate the same coefficient to an area entropy [4, 5, 6]. Finite quantum walks and causal networks supply explicit local, unitary microscopic histories [15, 16]. The unresolved conjunction is to realize these ingredients in one finite model that also reconstructs relational geometry, reduces to two tensor helicities, selects its global quantum sector, and produces a numerical Newton coupling from independently measured matter data.

We introduce an explicit hybrid finite causal cell. Eight body-centered-cubic route histories provide local unitary propagation, a recurrence coin opens a gapped occupied branch, and four Gauss-invariant ports provide the six relational data of a centered-Gram coframe. A compatible Cartan connection and ten plaquettes supply intrinsic geometry, while event-section and scalar constraints reduce the six-component shell to two tensor classes. The occupied source-target history is evaluated on a closed time path and generates source, retarded response, thresholds, and positive noise. Route, recurrence, and occupation variables are quantum; the coframe and connection are collective mean fields in the present calculation. We refer to the resulting source-target architecture as relational causal-flow dynamics (RCFD).

The derivation has three principal stages. First, the physical tensor, scalar-source, and static branches are shown to carry one finite normalization, eliminating the possibility of separate "wave" and "Newtonian" gravitational couplings. Second, a coframe-covariant Julia replica equation selects the

semiclassical capacity sector $K_* = 362$, for which

$$D_* = D_{362} = 107\,232\,946\,821. \tag{1}$$

Complete lower-branch occupation and the oriented three-slot coframe-volume channel then give the basis-independent reduction D_*^{-3}. Third, the model closes the remaining finite transfer by identifying its doubled determinant character with the positive electroweak scalar

$$\mathcal{R}_{\mathrm{EW}} = \frac{\alpha_{G_F}}{\alpha(0)} = \frac{\sqrt{2}\, G_F M_W^2 (1 - M_W^2/M_Z^2)}{\pi \alpha(0)}. \tag{2}$$

In the conventional G_F input scheme, this is the observable ratio conventionally written as $1 + \Delta r$ [21, 22, 23].

The centered-Gram shell is the six-dimensional space $\mathrm{Sym}^2(\mathbb{R}^3)$. Its forward and backward closed-time-path copies form a twelve-direction matching space. Multiplicativity under source-target gluing selects the determinant as its continuous scalar character, and least logarithmic history distributes a fixed determinant isotropically. The unique transfer is therefore

$$\mathcal{M}_{\mathrm{EW}} = \mathcal{R}_{\mathrm{EW}}^{1/12}. \tag{3}$$

Combining the horizon-selected rank, the filled-sea channel factor, and the electroweak transfer gives

$$\boxed{G_{\mathrm{pred}} = \frac{G_F}{\sqrt{2}\, D_{362}^3} \left[\frac{\sqrt{2}\, G_F M_W^2 (1 - M_W^2/M_Z^2)}{\pi \alpha(0)} \right]^{1/12}}. \tag{4}$$

Current electroweak inputs yield

$$G_{\mathrm{pred}} = 6.67484(28) \times 10^{-11}\ \mathrm{m^3\,kg^{-1}\,s^{-2}}, \tag{5}$$

which differs from the CODATA value by 1.72 combined standard deviations. This cross-sector relation is experimentally vulnerable in several independent ways: improved W- and Z-mass measurements change the predicted interval, complete horizon-edge accounting can move the selected capacity, and any noncentral coframe transfer would split the tensor shell and invalidate the least-history closure.

1.1. *Principal results and organization*

The principal results are:

(i) The finite route, recurrence, Gram, Cartan, and constraint data define a common two-helicity tensor sector with a positive occupied response.

(ii) The continuum tensor coefficient, source constraints, and direct BCC static Green function share one normalization.

(iii) Generalized horizon entropy selects the integer capacity $K_* = 362$.

(iv) Complete occupation and the three-slot oriented volume channel give the exact factor D_{362}^{-3}.

(v) The electroweak determinant closure, together with the determinant-character and least-history theorems, gives the unique central factor $\mathcal{R}_{\mathrm{EW}}^{1/12}$.

(vi) Equation (4) predicts G from G_F, $\alpha(0)$, M_W, and M_Z, with no gravitational parameter on the right-hand side.

Sections 2 and 3 develop the local model and gravitational normalization; Sections 4 and 5 derive the capacity and channel factors; Sections 6 and 7 construct the electroweak transfer; and Sections 9 to 12 and 15 give the prediction, structural alternatives, and experimental tests.

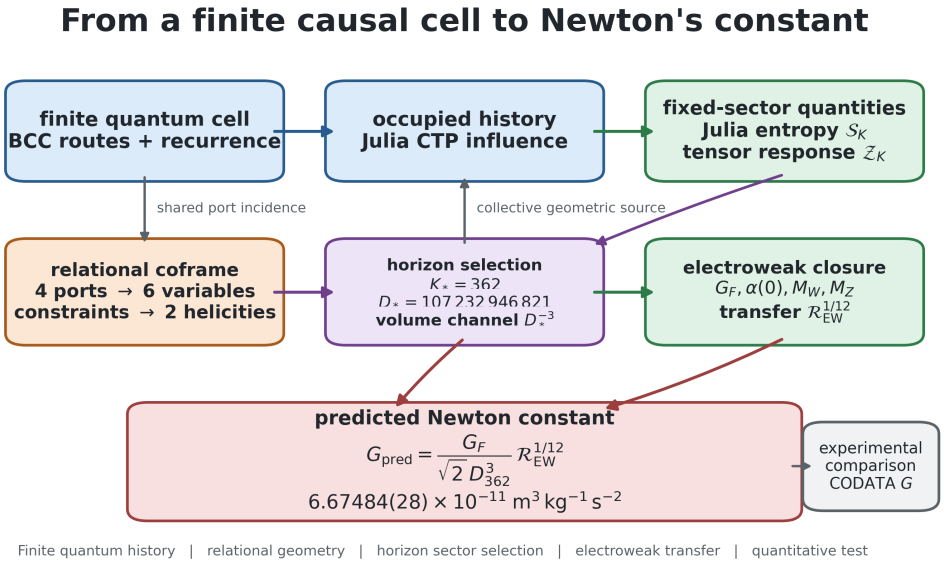


Figure 1: Logical structure of the calculation. The finite route and coframe sectors determine the fixed-capacity entropy and response. Horizon consistency selects $K_* = 362$ and D_{362}; complete occupation supplies D_{362}^{-3}; and the electroweak closure ratio fixes the central transfer $\mathcal{R}_{\mathrm{EW}}^{1/12}$. Their product gives the predicted Newton constant.

2. Hybrid finite causal-cell model

The local construction combines a parity-completed BCC route update, recurrence and occupation, a four-port centered-Gram geometry, Cartan transport, a relational constraint quotient, and a closed-time-path occupied influence. Their compatibility under one source-target composition law defines the finite cell used throughout the calculation.

Definition 2.1 (Hybrid finite causal-cell model)**.** On an oriented event graph $\mathcal{G} = (V, E)$, define

$$\mathfrak{M}_{\mathrm{cell}} = (\Lambda_{\mathrm{BCC}}, U_m, \mathcal{H}_{\mathrm{Gram}}^{(K)}, P_-, \bar{G}, E, \omega, S_{\mathrm{EC}}^{(d)}, \Gamma_{\mathrm{occ}}, \mathcal{C}_{\mathrm{rel}}). \tag{6}$$

The entries and their required compatibility conditions are:

(i) **Causal route process.** Each oriented edge carries a finite unitary route update. In the branch used here, eight BCC body-diagonal histories re-

produce a parity-completed Weyl process in the principal long-wavelength valley.

(ii) **Recurrence and occupation.** Complementary chiral routes are mixed by a finite recurrence coin. A gapped lower branch is filled by an occupied projector P_-; empty partner states provide the virtual transitions entering response.

(iii) **Relational coframe.** Four closed spatial ports satisfy a Gauss condition. Their centered Gram data determine six spatial metric variables, a positive metric q, and a coframe E modulo one common local rotation.

(iv) **Cartan-soldered curvature.** A time normal extends E to a tetrad. Metric-compatible link transport and ten port-resolved plaquettes reconstruct curvature. The intrinsic geometric phase is the discrete boundary-completed Einstein–Cartan phase $S_{\mathrm{EC}}^{(d)}$.

(v) **Constraint quotient.** Event-section changes and one scalar-capacity functional form a complex. At nonzero incidence, the physical spatial shell is its two-dimensional cohomology, not the unreduced six-component shell.

(vi) **Occupied quantum influence.** Source and target coframes enter the occupied route history through their relative cofactor. The closed-time-path influence Γ_{occ} generates mean source, retarded response, dissipation and noise; it is not identified with the intrinsic Einstein–Cartan phase.

(vii) **Finite-band and global closure.** The exact compact-frequency kernel, not only its derivative expansion, determines physical poles and thresholds. A global horizon condition may select the integer capacity sector that local capacity-preserving dynamics cannot choose.

The layers share the same route incidence, coframe, source-target arrow, and physical quotient.

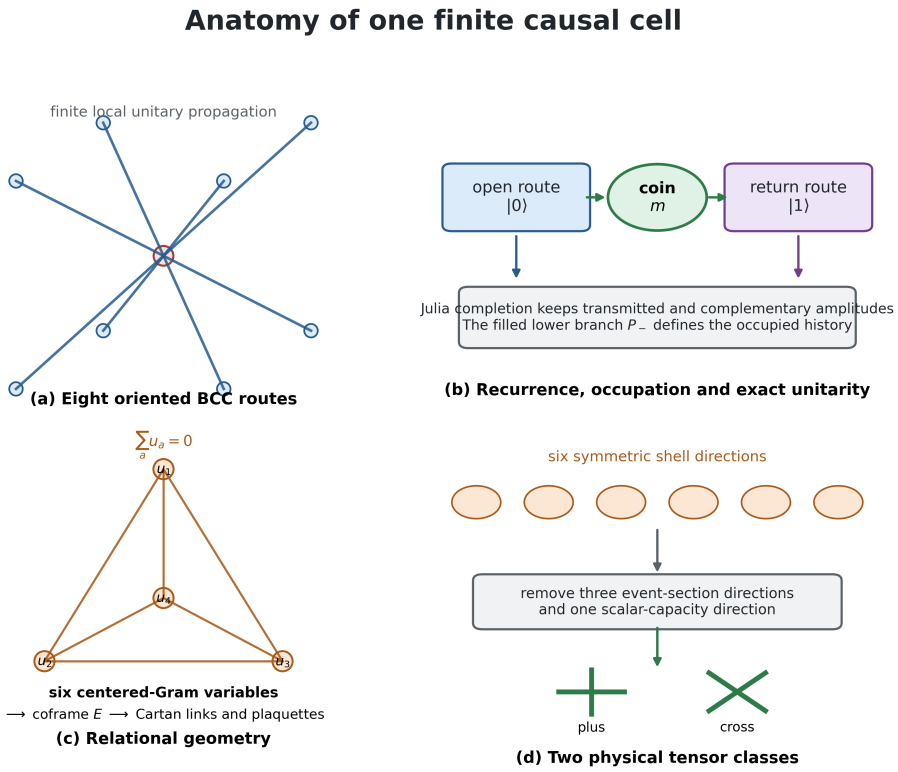


Figure 2: Anatomy of one finite causal cell. (a) Eight BCC routes provide local propagation. (b) The recurrence coin and Julia completion retain both transmitted and complementary amplitudes; filling the lower branch defines the occupied history. (c) Four Gauss-closed ports reconstruct six centered-Gram variables, a coframe and Cartan transport. (d) Three event-section directions and one scalar-capacity direction are removed, leaving the plus and cross tensor classes. Intrinsic Cartan geometry supplies the phase, whereas the occupied relative-cofactor history supplies source, response, thresholds and noise.

The corresponding hybrid closed-time-path functional is schematically

$$\boxed{\Gamma_{\mathrm{RCFD}}[e^{\pm},\omega^{\pm};P_-] = S^{(d)}_{\mathrm{EC}}[e^{+},\omega^{+}] - S^{(d)}_{\mathrm{EC}}[e^{-},\omega^{-}] + \Gamma_{\mathrm{occ}}[\mathfrak{R}^{+},\mathfrak{R}^{-};P_-].} \tag{7}$$

Here $e^{\pm}$ and $\omega^{\pm}$ are the forward/backward collective tetrad and Cartan connection, and P_- is the quantum occupied projector. For a spatial coframe E, define the cofactor frame

$$F(E) = \det(E)E^{-\mathsf{T}} \tag{8}$$

and the source-target relative cofactor

$$\mathfrak{R}_{t\leftarrow s} = F(E_s)^{-1}F(E_t). \tag{9}$$

The intrinsic term in (7) governs geometric propagation and constraints. The occupied term generates matter source, polarization, thresholds, dissipation, and fluctuations. Their sum couples a Lorentzian geometric phase to a positive quantum influence without identifying the two structures.

Table 1: Components of the finite causal-cell model and their roles in the Newton-closure theorem.

Layer	**Primitive finite object**	**Role in the closure**
Causal kinematics	BCC source-target routes and parity-completed Weyl update	One common principal causal cone and the route moment identity.
Persistence	Recurrence coin and occupied lower branch	The selected angle m_K, occupied projector and finite rank D_K.
Relational geometry	Four Gauss-closed ports and centered Gram data	A complete six-component spatial shell, coframe and cofactor area.
Soldered curvature	Cartan link and ten plaquettes	The intrinsic Einstein–Cartan phase and its tensor normalization.
Constraint reduction	Event-section map and scalar-capacity functional	The two-dimensional physical tensor cohomology.
Quantum influence	Relative Port–Julia history on a closed time path	$\mathcal{S}_K$, $\mathcal{Z}_K$, source rigidity, thresholds and positive noise.
Finite/global closure	Exact band, horizon algebra and capacity charge	The sector $K_* = 362$ and the finite matching problem solved below.

2.1. Quantum and collective sectors

The route amplitudes, recurrence register, Gauss channels, and occupied projector are quantum. The coframe and Cartan connection in (7) are collective mean fields reconstructed from the quantum Gram data. We work

on the spin-saturated tensor branch, where the mean torsion vanishes and the compatible connection reduces to the Levi–Civita branch.

The branch used below fixes the BCC route set, a spin-summed four-valent $SU(2)$ Gauss tower truncated by an integer capacity K, complete occupation of its lower branch, the coframe-normal horizon algebra, and the positive determinant/least-history electroweak matching law. The equality $\mathcal{Z}_{\mathrm{geom}} = \mathcal{Z}_{\mathrm{horizontal}}$ is required only for the microscopic event-length estimates in Section 13; the direct Fermi–Newton relation is independent of that specialization.

3. Finite cell, coframe and occupied Gauss tower

3.1. BCC routes and coframe geometry

The local routing graph uses the eight oriented body diagonals

$$\mathcal{R}_8 = \{(\pm 1, \pm 1, \pm 1)\}. \tag{10}$$

They satisfy

$$\sum_{\boldsymbol{r}\in\mathcal{R}_8} \boldsymbol{r} = 0, \qquad \frac{1}{8}\sum_{\boldsymbol{r}\in\mathcal{R}_8} \boldsymbol{r}\boldsymbol{r}^{\mathsf{T}} = I_3. \tag{11}$$

The first identity gives directional closure; the second makes the quadratic route symbol isotropic. The four unoriented tetrahedral representatives may be assembled as

$$T = \frac{1}{\sqrt{3}}\begin{pmatrix} 1 & 1 & 1 \\ 1 & -1 & -1 \\ -1 & 1 & -1 \\ -1 & -1 & 1 \end{pmatrix}, \qquad T^{\mathsf{T}}T = \frac{4}{3}I_3, \qquad T^{\mathsf{T}}\mathbf{1} = 0. \tag{12}$$

Proposition 3.1 (Exact centered-Gram reconstruction)**.** *Let $C \in \mathrm{Sym}^{+}(3)$ be the positive cofactor metric and define the four-port centered Gram record*

$$G = TCT^{\mathsf{T}}. \tag{13}$$

Then $G\mathbf{1} = 0$, $\operatorname{rank} G = 3$, and

$$\boxed{C = \frac{9}{16}T^{\mathsf{T}}GT.} \tag{14}$$

The spatial metric and coframe are recovered as

$$q = (\det C)^{1/2} C^{-1}, \qquad q = E^{\mathsf{T}} E, \tag{15}$$

where E is unique up to left multiplication by $SO(3)$. Thus the six-dimensional cone of positive centered Gram records is exactly the local spatial metric shell modulo frame rotation.

Proof. Equation (12) gives $T^{\mathsf{T}} G T = (T^{\mathsf{T}} T) C (T^{\mathsf{T}} T) = 16C/9$, proving (14). For $C = \det(q) q^{-1}$ in three dimensions, $\det C = (\det q)^2$, which gives (15). Positive square roots differ by one orthogonal rotation; orientation restricts it to $SO(3)$. □

The source-target variable is relational rather than an absolute cofactor measured from a preferred identity frame. For the symmetric split

$$E_s = E_0 e^{-h/2}, \qquad E_t = E_0 e^{h/2}, \qquad h = h^{\mathsf{T}}, \tag{16}$$

(9) gives the exact cancellation

$$\boxed{\mathfrak{R}_{t \leftarrow s} = e^{(\operatorname{Tr} h) I - h},} \tag{17}$$

independent of the common positive background E_0. This is why the model uses a relative-cofactor Port–Julia influence: all constant coframes have one local law in their own orthonormal coordinates.

One connected BCC component has primitive coordinate volume

$$v_0 = 4a^3 \tag{18}$$

in a local orthonormal frame. For a horizon section with normal covector n and spatial metric q, the physical coframe area density is

$$\mu_q(n) = \sqrt{\det q}\, \sqrt{n^{\mathsf{T}} q^{-1} n}. \tag{19}$$

Equal counting of raw links gives an orientation-dependent crystalline norm; the quadratic port weights inherited from (11) give (19) and match the leading tensor response.

3.2. Four-valent Gauss tower

At total four-port Gauss area J, the invariant multiplicity is [9]

$$d_J = \frac{(J+1)(J+2)^2(J+3)}{12}. \tag{20}$$

A capacity sector K contains $J = 0, \ldots, K$. The occupied lower-branch rank is

$$\boxed{D_K = \sum_{J=0}^{K} d_J = \frac{(K+1)(K+2)(K+3)(K+4)(2K+5)}{120}.} \tag{21}$$

Particle–hole completion doubles the full one-particle fiber, but it does not double the number of occupied lower-branch channels. This distinction is important below: the channel trace uses D_K, whereas $2D_K$ is a different structural hypothesis and gives a very different numerical result.

3.3. Coin-selected recurrence margin

For a fixed K, introduce

$$0 < \xi < \frac{1}{\sqrt{2}}, \qquad m_K(\xi) = \arccos\frac{\xi}{K+1}. \tag{22}$$

Let

$$u_J = \frac{J+1}{\sqrt{1+(J+1)^2}}, \qquad y_K(\xi) = \sqrt{1 - \frac{\xi^2}{(K+1)^2}}, \tag{23}$$

and

$$\alpha_{J,K}(\xi) = 2\arcsin[u_J y_K(\xi)]\,. \tag{24}$$

The finite collective-coin functional is

$$W_K(\xi) = \sum_{J=0}^{K} d_J\Big[\alpha_{J,K}(0) - \alpha_{J,K}(\xi)\Big] - 2d_K m_K(\xi)\xi\sqrt{1-\xi^2}. \tag{25}$$

Its unique interior stationary minimum is denoted ξ_K. The deterministic calculation brackets the root of $W_K'(\xi)$ on $(0, 1/\sqrt{2})$.

3.4. Julia entropy and horizontal tensor response

At level J define

$$t_{J,K} = \left(\frac{(J+1)\xi_K}{K+1} \right)^2, \qquad p_{J,K} = \frac{t_{J,K}}{1+t_{J,K}}. \tag{26}$$

The endpoint Julia state is

$$|\Omega_{J,K}\rangle = \frac{|1\rangle_s|0\rangle_t - \sqrt{t_{J,K}}|0\rangle_s|1\rangle_t}{\sqrt{1+t_{J,K}}}. \tag{27}$$

Tracing one endpoint gives binary entropy

$$h(p) = -p\ln p - (1-p)\ln(1-p), \tag{28}$$

and the complete tower entropy is

$$\boxed{\mathcal{S}_K = \sum_{J=0}^{K} d_J h(p_{J,K}).} \tag{29}$$

The same occupied graph projector gives connected horizontal response

$$z(t) = \frac{t(1-t)}{(1+t)^3}, \qquad \boxed{\mathcal{Z}_K = \sum_{J=0}^{K} d_J z(t_{J,K}).} \tag{30}$$

Entropy and response are different spectral functions, but they use precisely the same occupied channels and multiplicities.

3.5. Relational constraint complex and two-helicity quotient

Let $\boldsymbol{\kappa} \neq 0$ be the spatial incidence covector of one Fourier or finite-incidence mode, and let $h \in \mathrm{Sym}^2(\mathbb{C}^3)$ be a shell deformation. An infinitesimal event-section change $\boldsymbol{\xi} \in \mathbb{C}^3$ acts by

$$(G_{\boldsymbol{\kappa}}\boldsymbol{\xi})_{ij} = \mathrm{i}(\kappa_i\xi_j + \kappa_j\xi_i), \tag{31}$$

and the scalar-capacity functional is

$$Q_{\boldsymbol{\kappa}}h = (\kappa_i\kappa_j - |\boldsymbol{\kappa}|^2\delta_{ij})h_{ij}. \tag{32}$$

Direct contraction gives

$$Q_{\boldsymbol{\kappa}}G_{\boldsymbol{\kappa}} = 0. \tag{33}$$

Proposition 3.2 (Two-helicity relational quotient)**.** *For $\boldsymbol{\kappa} \neq 0$, the physical shell*

$$\boxed{\mathcal{H}_{\mathrm{phys}}(\boldsymbol{\kappa}) = \ker Q_{\boldsymbol{\kappa}} / \operatorname{im} G_{\boldsymbol{\kappa}}} \tag{34}$$

has complex dimension two.

Proof. The map $G_{\boldsymbol{\kappa}}$ has rank three and the nonzero functional $Q_{\boldsymbol{\kappa}}$ has rank one. Hence $\dim \ker Q_{\boldsymbol{\kappa}} = 5$. Equation (33) places the three-dimensional image of $G_{\boldsymbol{\kappa}}$ inside that kernel, giving dimension $5 - 3 = 2$. In a frame with $\boldsymbol{\kappa} \parallel \hat{z}$, representatives may be chosen as $h_{xx} = -h_{yy}$ and $h_{xy} = h_{yx}$, the plus and cross tensor patterns. □

The six centered-Gram directions are therefore the complete local geometry coordinates, not six propagating gravitons. All response and matching operators must be applied to the full shell before the quotient, while physical pole counting is performed on (34).

3.6. Continuum Newton normalization

Let $\mathcal{Z}_{\mathrm{IR}}$ denote the coefficient of the complete quadratic tensor shell after the chosen intrinsic/horizontal bookkeeping. On the two physical helicities the finite action is

$$\frac{S^{(2)}_{\mathrm{RCFD}}}{\hbar} = \frac{\mathcal{Z}_{\mathrm{IR}}}{2} \sum_{n,v} \left[|h_{n+1,v} - h_{n,v}|^2 - \frac{1}{8} \sum_{\boldsymbol{r} \in \mathcal{R}_8} |h_{n,v+\boldsymbol{r}} - h_{n,v}|^2 \right]. \tag{35}$$

With $t = n\tau$, $x = av$, $c = a/\tau$ and

$$\sum_{n,v} \longrightarrow \frac{1}{\tau v_0} \int \mathrm{d}t\, \mathrm{d}^3x, \tag{36}$$

the route moment identity (11) gives

$$S^{(2)}_{\mathrm{RCFD}} \longrightarrow \frac{\hbar \mathcal{Z}_{\mathrm{IR}} a^2}{2\tau v_0} \int \mathrm{d}t\, \mathrm{d}^3x \left[\frac{1}{c^2} |\dot{h}|^2 - |\nabla h|^2 \right]. \tag{37}$$

The orthonormal transverse-traceless Einstein normalization is

$$S^{\mathrm{TT}}_{\mathrm{EH}} = \frac{c^4}{64\pi G} \int \mathrm{d}t\, \mathrm{d}^3x \left[\frac{1}{c^2} |\dot{h}|^2 - |\nabla h|^2 \right]. \tag{38}$$

following the standard ADM/DeWitt normalization [11, 12]. Therefore

$$\boxed{G = \frac{c^3 v_0}{32\pi\hbar a \mathcal{Z}_{\mathrm{IR}}}.} \tag{39}$$

For the primitive event convention $v_0 = 4a^3$,

$$\frac{\hbar G}{c^3 a^2} = \frac{1}{8\pi \mathcal{Z}_{\mathrm{IR}}}. \tag{40}$$

Equation (39) defines the conventional Newton normalization of the finite tensor coefficient; the next theorem shows that it is not merely a wave-sector conversion.

3.7. Exact source-normalization rigidity

Let p be conjugate to h. The linear canonical maps obey

$$\dot{h} = \mathcal{Z}_{\mathrm{IR}}^{-1}\mathsf{M}p + G_{\boldsymbol{\kappa}}\boldsymbol{\beta}, \qquad \dot{p} = -\mathcal{Z}_{\mathrm{IR}}\mathsf{K}_{\boldsymbol{\kappa}}h - \Theta, \tag{41}$$

where Θ is the occupied shell stress. The finite maps are characterized, for the normalization argument, by

$$Q_{\boldsymbol{\kappa}}G_{\boldsymbol{\kappa}} = 0, \qquad G_{\boldsymbol{\kappa}}^{\mathsf{T}}\mathsf{K}_{\boldsymbol{\kappa}} = 0, \tag{42}$$

$$Q_{\boldsymbol{\kappa}}\mathsf{M} = \frac{1}{2}\boldsymbol{\kappa}^{\mathsf{T}}G_{\boldsymbol{\kappa}}^{\mathsf{T}}, \qquad \frac{1}{2}G_{\boldsymbol{\kappa}}^{\mathsf{T}}\Theta = \Theta\boldsymbol{\kappa}. \tag{43}$$

Start with independently normalized scalar and momentum constraints,

$$\mathcal{C}_0 = a_0 Q_{\boldsymbol{\kappa}}h - \varepsilon, \qquad \boldsymbol{\mathcal{C}} = b_0 G_{\boldsymbol{\kappa}}^{\mathsf{T}}p - \boldsymbol{j}, \tag{44}$$

for sources satisfying

$$\dot{\varepsilon} = \boldsymbol{\kappa}\cdot\boldsymbol{j}, \qquad \dot{\boldsymbol{j}} = -\Theta\boldsymbol{\kappa}. \tag{45}$$

Differentiating (44) with (41)–(43) gives

$$\dot{\mathcal{C}}_0 = \frac{a_0}{2b_0\mathcal{Z}_{\mathrm{IR}}}\boldsymbol{\kappa}\cdot\boldsymbol{\mathcal{C}} + \left(\frac{a_0}{2b_0\mathcal{Z}_{\mathrm{IR}}} - 1\right)\boldsymbol{\kappa}\cdot\boldsymbol{j}, \tag{46}$$

$$\dot{\boldsymbol{\mathcal{C}}} = -(2b_0 - 1)\Theta\boldsymbol{\kappa}. \tag{47}$$

Theorem 3.3 (Source-normalization rigidity)**.** *Constraint propagation for every locally conserved source holds if and only if*

$$\boxed{a_0 = \mathcal{Z}_{\mathrm{IR}}, \qquad b_0 = \frac{1}{2}.} \tag{48}$$

Thus the physical tensor action, scalar source and momentum source cannot carry independently adjustable dimensionless gravitational normalizations.

Proof. The source-contamination terms in (46) and (47) vanish for arbitrary $\boldsymbol{j}$ and Θ exactly under (48). Conversely, any other values leave a nonzero term for a conserved source. □

3.8. Direct static branch

On one connected BCC component define

$$(L_{\mathrm{BCC}} f)_v = 2f_v - \frac{1}{4} \sum_{\boldsymbol{r} \in \mathcal{R}_8} f_{v+\boldsymbol{r}}. \tag{49}$$

Its symbol is

$$\lambda(\boldsymbol{q}) = 2[1 - \cos q_x \cos q_y \cos q_z]. \tag{50}$$

It has four coherent quadratic valleys on the source component [14], and hence

$$\boxed{G_{\mathrm{BCC}}(v) = \frac{1}{\pi |v|} + O(|v|^{-3}).} \tag{51}$$

In the time-symmetric conformal branch $q_{ij} = \phi^4 \delta_{ij}$, the sourced finite-cell constraint is

$$\boxed{8\mathcal{Z}_{\mathrm{IR}}\, \phi L_{\mathrm{BCC}} \phi = \varepsilon.} \tag{52}$$

For nonnegative source and positive Dirichlet boundary data it is the stationary equation of

$$\mathcal{J}[u] = 4\mathcal{Z}_{\mathrm{IR}} \langle u, L_D u \rangle - \sum_v v_0 \varepsilon_v \log(1 + u_v), \qquad \phi = 1 + u, \tag{53}$$

whose Hessian is strictly positive. The positive solution is unique, in direct analogy with the conformal initial-value construction [13], and has far field

$$\phi(r) = 1 + \frac{\mathcal{E}_{\mathrm{eff}}}{32\pi \mathcal{Z}_{\mathrm{IR}} r} + O(r^{-3}). \tag{54}$$

Thus the same coefficient fixed by the tensor action and source-rigidity theorem governs a direct inverse-distance static branch. Identifying the cell-normalized ε with a realistic matter density is a matter-sector dictionary, not an additional gravitational coupling.

4. Horizon selection of the global capacity sector

4.1. Replica identity

For a graph operator T with $X = T^\dagger T$, the filled Gaussian graph state has reduced replica function

$$\operatorname{Tr} \rho_s^n = \frac{\det(I + X^n)}{\det(I + X)^n}. \tag{55}$$

For $X_{J,K} = t_{J,K} I_{d_J}$,

$$\operatorname{Tr} \rho_{s,K}^n = \prod_{J=0}^{K} \left[\frac{1 + t_{J,K}^n}{(1 + t_{J,K})^n} \right]^{d_J}, \tag{56}$$

whose replica derivative reproduces (29). On an affine coframe-normal horizon, the Julia entropy density is

$$\frac{S_{\text{Julia}}}{A_q} = \frac{\mathcal{S}_K}{a^2}. \tag{57}$$

For a smooth curved section, the finite coarea construction gives a relative correction of order $a^2/\mathcal{R}_\Sigma^2$.

4.2. Generalized-entropy accounting

Write the infrared two-derivative coefficient as

$$\mathcal{Z}_{\text{IR}} = \mathcal{Z}_{\text{geom}} + \mathcal{Z}_{\text{horizontal}}. \tag{58}$$

The explicit generalized entropy contains the intrinsic Wald term plus the Julia entropy, whereas the infrared Wald expression contains both coefficients. Equality gives

$$\frac{2\pi \mathcal{Z}_{\text{geom}} + \mathcal{S}_K}{a^2} = \frac{2\pi(\mathcal{Z}_{\text{geom}} + \mathcal{Z}_{\text{horizontal}})}{a^2}, \tag{59}$$

so the intrinsic term cancels and

$$\boxed{\mathcal{S}_K = 2\pi \mathcal{Z}_{\text{horizontal,K}}.} \tag{60}$$

This is analogous in spirit to induced-gravity and horizon-entanglement relations [1, 2, 3, 4, 5, 6], while remaining a finite model equation rather than a regulator limit.

Theorem 4.1 (Horizon-selected high-capacity sector)**.** *For the coin-selected tower* (25)–(30)*, define*

$$\epsilon_K = 1 - \frac{\mathcal{S}_K}{2\pi \mathcal{Z}_K}. \tag{61}$$

The finite spectrum has sign changes between $K = 2, 3$ *and* $K = 361, 362$*. On the semiclassical branch* $\mathcal{Z}_K \gg 1$*, the continuous root is*

$$K_c = 361.542964\ldots, \tag{62}$$

and the unique integer minimizer of $|\epsilon_K|$ *is*

$$\boxed{K_* = 362.} \tag{63}$$

The selected data are

$$\begin{aligned} D_* &= 107232946821, \\ \xi_* &= 0.6903899851287184957\ldots, \\ m_* &= 1.5688944248628151716\ldots, \\ \mathcal{Z}_* &= 9.403555918789965632 \times 10^9, \\ \mathcal{S}_* &= 5.908423961020760773 \times 10^{10}, \end{aligned} \tag{64}$$

with

$$\epsilon_* = 7.577983826 \times 10^{-7}. \tag{65}$$

4.3. Hybrid Newton normalization in causal units

The general continuum conversion was derived in (39). Theorem 3.3 and (54) show that the same coefficient governs the tensor, source, and static branches. The direct Fermi relation below does not require a choice of the intrinsic coefficient. Inferring the microscopic event length does. In the minimal equal-coefficient hybrid branch,

$$\mathcal{Z}_{\text{geom}} = \mathcal{Z}_{\text{horizontal}} = \mathcal{Z}_*, \qquad \mathcal{Z}_{\text{IR}} = 2\mathcal{Z}_*. \tag{66}$$

Equations (40) and (66) give

$$\widehat{G}_* \equiv \frac{\hbar G}{c^3 a^2} = \frac{1}{16\pi \mathcal{Z}_*} = 2.115621798636243 \times 10^{-12}, \tag{67}$$

$$\alpha_* \equiv \frac{G M_{\text{rec}}^2}{\hbar c} = \widehat{G}_* \sin^2 m_* = 2.115614145952802 \times 10^{-12}, \tag{68}$$

where $M_{\text{rec}} = \hbar \sin m_*/(ca)$. These are dimensionless predictions inside the specified hybrid branch.

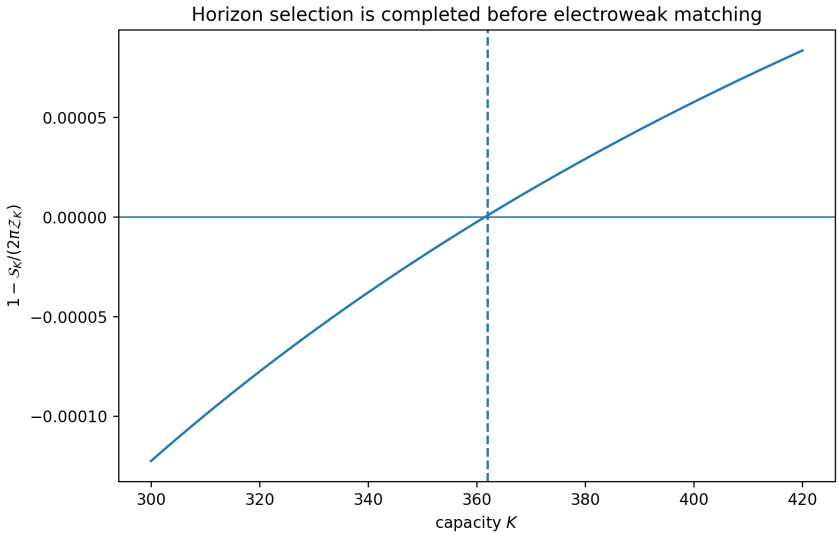


Figure 3: High-capacity generalized-entropy crossing. The continuous root lies between 361 and 362, and the integer sector minimizing the defect is $K = 362$.

5. Filled-sea channel theorem

5.1. Complete lower-branch occupation

Let the occupied channel space in sector K be

$$\mathcal{H}_K = \bigoplus_{J=0}^{K} \mathbb{C}^{d_J} \cong \mathbb{C}^{D_K}, \tag{69}$$

with fermionic operators $c_A, c_A^\dagger$, $A = 1, \ldots, D_K$. Complete lower-branch occupation is the Slater state

$$|\mathrm{Sea}_K\rangle = c_1^\dagger c_2^\dagger \cdots c_{D_K}^\dagger |0\rangle. \tag{70}$$

Lemma 5.1 (Filled-sea correlation)**.** *The one-body correlation matrix of* (70) *is*

$$C_{AB} = \langle \mathrm{Sea}_K | c_B^\dagger c_A | \mathrm{Sea}_K \rangle = \delta_{AB}. \tag{71}$$

Therefore the normalized channel-unresolved one-body state is

$$\boxed{\rho_{\mathrm{ch},K} = \frac{C}{\operatorname{Tr} C} = \frac{I_{D_K}}{D_K}.} \tag{72}$$

Proof. Every lower-branch mode is occupied exactly once. Hence c_A removes one occupied mode and $c_B^\dagger$ restores the state only when $A = B$. The trace is the occupied rank D_K. □

Equation (72) is invariant under occupied-basis rotations. The Julia probabilities may vary among J blocks, while complete occupation keeps the correlation projector equal to the identity on the occupied subspace.

Theorem 5.2 (Unique invariant channel functional)**.** *Let ρ be a density operator on $(\mathbb{C}^D)^{\otimes n}$ satisfying*

$$(U_1 \otimes \cdots \otimes U_n)\rho(U_1 \otimes \cdots \otimes U_n)^\dagger = \rho \tag{73}$$

for every $U_j \in U(D)$. Then

$$\boxed{\rho = \frac{I_{D^n}}{D^n}.} \tag{74}$$

Consequently every rank-r projector P_r has invariant weight

$$\mathrm{Tr}(\rho P_r) = \frac{r}{D^n}. \tag{75}$$

Proof. The defining representation of $U(D)$ is irreducible. The commutant of the independent product action $U(D)^n$ on $(\mathbb{C}^D)^{\otimes n}$ is therefore the scalar algebra. Hence $\rho = cI$. Unit trace fixes $c = D^{-n}$. □

Complete lower-branch occupation realizes the one-slot case of Theorem 5.2. Three independent coframe slots realize $n = 3$. It is the unique normalized channel functional compatible with independent occupied-basis covariance.

5.2. Why the volume channel has three ordered slots

Proposition 5.3 (Unique local oriented volume form)**.** *Let $V \simeq \mathbb{R}^3$ carry the oriented spatial coframe representation. The space of alternating trilinear $SO(3)$-invariant forms on V is one-dimensional. Every local orientation-preserving multilinear scalar formed from three coframe legs is therefore proportional to*

$$\varepsilon(v_1, v_2, v_3) = \epsilon_{abc} v_1^a v_2^b v_3^c. \tag{76}$$

Proof. Alternating trilinear forms constitute $\Lambda^3 V^*$. In three dimensions this space is one-dimensional, and proper rotations preserve its orientation generator. Any such invariant is therefore a scalar multiple of the volume form. □

The three entries of (76) are distinguishable tangent slots. Their ordering carries orientation; they are not three identical fermions selected from one channel register. This fixes the tensor-product structure used below independently of the numerical comparison with G.

5.3. Three ordered coframe slots

The local oriented volume is trilinear,

$$\mathcal{V} = e^1 \wedge e^2 \wedge e^3. \tag{77}$$

The spatial labels $1, 2, 3$ are ordered tangent slots, not three identical fermion labels. The channel space for a primitive ordered volume insertion is therefore

$$\mathcal{H}_K^{(1)} \otimes \mathcal{H}_K^{(2)} \otimes \mathcal{H}_K^{(3)}, \tag{78}$$

and the channel-unresolved density is

$$\rho_{\mathrm{ch},K}^{(3)} = \rho_{\mathrm{ch},K} \otimes \rho_{\mathrm{ch},K} \otimes \rho_{\mathrm{ch},K} = \frac{I_{D_K^3}}{D_K^3}. \tag{79}$$

Let $|\mathbb{V}_K\rangle$ be any normalized geometry-active oriented-volume state in this ordered channel space, and let

$$\Pi_{\mathbb{V},K} = |\mathbb{V}_K\rangle\langle\mathbb{V}_K| \tag{80}$$

be its rank-one projector.

Theorem 5.4 (Basis-independent channel trace)**.** *For complete lower-branch occupation and three ordered coframe slots,*

$$\boxed{\mathrm{Tr}\left(\rho_{\mathrm{ch},K}^{(3)} \Pi_{\mathbb{V},K}\right) = D_K^{-3}.} \tag{81}$$

The result is independent of the basis and of the detailed normalized coefficients of $|\mathbb{V}_K\rangle$*.*

Proof. Using (79) and $\mathrm{Tr}\,\Pi_{\mathbb{V},K} = 1$,

$$\mathrm{Tr}\left(\rho_{\mathrm{ch},K}^{(3)} \Pi_{\mathbb{V},K}\right) = D_K^{-3}\,\mathrm{Tr}\,\Pi_{\mathbb{V},K} = D_K^{-3}. \tag{82}$$

For $U_a \in U(D_K)$, $\rho_{\mathrm{ch},K}^{(3)}$ commutes with $U_1 \otimes U_2 \otimes U_3$, so the trace is basis invariant. □

This theorem is stronger and cleaner than a coherent democratic-state calculation. It shows that the power D^{-3} follows from full occupation, channel-unresolved tracing, three ordered tangent slots, and a rank-one volume channel.

5.4. Exact controlled-volume reduction

The channel trace can be implemented dynamically rather than appended as a probability factor. Let $\mathcal{H}_M$ be any finite matter/source register, let $O = O^\dagger$ act on it, and define the controlled unitary

$$U_\varepsilon = (I - \Pi_{\mathbb{V},K}) \otimes I_M + \Pi_{\mathbb{V},K} \otimes e^{-\mathrm{i}\varepsilon O}. \tag{83}$$

Theorem 5.5 (Controlled-volume gate)**.** *For channel state $\rho^{(3)}_{\mathrm{ch},K} = I/D_K^3$, the reduced matter map generated by (83) is exactly*

$$\Phi_\varepsilon(\sigma) = \left(1 - D_K^{-3}\right)\sigma + D_K^{-3} e^{-\mathrm{i}\varepsilon O}\sigma e^{\mathrm{i}\varepsilon O}. \tag{84}$$

Its coherent infinitesimal generator is

$$\left.\frac{\mathrm{d}}{\mathrm{d}\varepsilon}\Phi_\varepsilon(\sigma)\right|_0 = -\mathrm{i}D_K^{-3}[O,\sigma]. \tag{85}$$

Proof. The two orthogonal channel sectors $\Pi_{\mathbb{V},K}$ and $I - \Pi_{\mathbb{V},K}$ are classical alternatives after tracing the channel register. Their probabilities are D_K^{-3} and $1 - D_K^{-3}$ by Theorem 5.4. Equation (84) follows directly, and differentiation gives (85). □

The same finite gate also predicts a second cumulant proportional to $D_K^{-3}(1 - D_K^{-3})$. Thus the leading coherent coefficient and the channel-induced fluctuation are not independently adjustable. This feature will become relevant if the electroweak/coframe completion is constructed as a closed-time-path influence rather than only as a tree-level matching.

5.5. Countermodel: three identical channels from one sea

If the three labels were instead identical fermions drawn from one channel sea, the natural space would be $\Lambda^3\mathcal{H}_K$, of dimension $\binom{D_K}{3}$. A maximally mixed state on that space would give

$$\mathrm{Tr}(\rho_{\Lambda^3}\Pi) = \binom{D_K}{3}^{-1} \sim \frac{6}{D_K^3}, \tag{86}$$

rather than D_K^{-3}. The factor-of-six difference changes the predicted Newton constant by the same factor, so the ordered-slot structure is a direct test of the volume-channel construction.

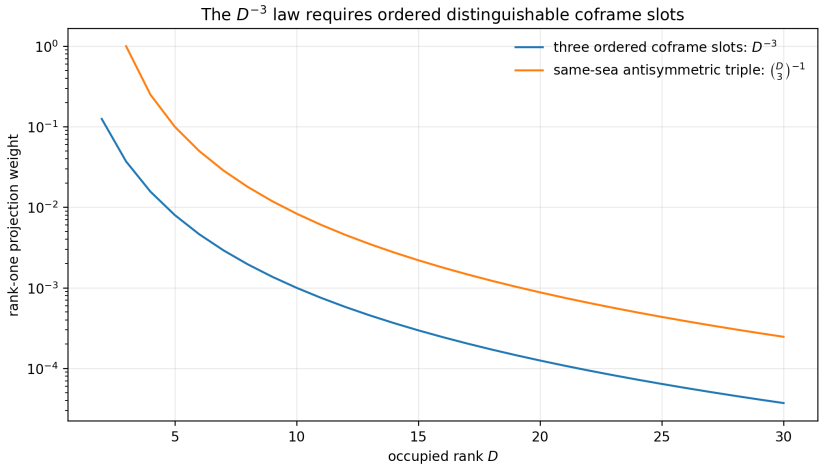


Figure 4: Ordered-slot and same-sea alternatives. The exact D^{-3} law belongs to three distinguishable coframe slots. Treating the labels as three identical fermions produces $\binom{D}{3}^{-1}$ instead.

6. Electroweak closure scalar

6.1. A dimensionless quantity with no gravitational input

The low-energy charged-current interaction is conventionally normalized as

$$\mathcal{L}_F = -\frac{G_F}{\sqrt{2}}\, J_L^{\mu\dagger} J_{L\mu}. \tag{87}$$

The Fermi constant is extracted from the muon lifetime after finite-mass and QED effects are included [17, 18, 19, 20]. Define the on-shell weak angle

$$s_W^2 = 1 - \frac{M_W^2}{M_Z^2} \tag{88}$$

and the G_F-scheme electromagnetic normalization

$$\alpha_{G_F} = \frac{\sqrt{2}\, G_F M_W^2 s_W^2}{\pi}. \tag{89}$$

The positive closure scalar is

$$\boxed{\mathcal{R}_{\rm EW} = \frac{\alpha_{G_F}}{\alpha(0)} = \frac{\sqrt{2}\, G_F M_W^2 (1 - M_W^2/M_Z^2)}{\pi \alpha(0)}.} \tag{90}$$

It is built entirely from non-gravitational observables. In the G_F input scheme it equals $1 + \Delta r$ in the plus convention [22, 23]. The ratio packages the finite transition from the Thomson-limit electromagnetic normalization to the charged-current normalization. Using the full observable ratio avoids a scheme-dependent subdivision into loop subclasses.

Using the input values in (94),

$$G_F = 1.1663787(6) \times 10^{-5}\ \mathrm{GeV}^{-2}, \tag{91}$$

$$\alpha(0)^{-1} = 137.035999177(21), \tag{92}$$

$$M_W = 80.3625(77)\ \mathrm{GeV}, \tag{93}$$

$$M_Z = 91.1879(20)\ \mathrm{GeV}, \tag{94}$$

one obtains

$$\boxed{\mathcal{R}_{\mathrm{EW}} = 1.0377852947590087.} \tag{95}$$

The W and Z masses are the 2026 Particle Data Group values [24, 25, 26]; G_F and $\alpha(0)$ are the 2022 CODATA values [30].

6.2. Why the observable ratio, rather than a named loop term

The decomposition of Δr depends on renormalization convention, input scheme, and perturbative organization. By contrast, (90) is a direct ratio of measured electroweak normalizations in the on-shell mass convention. The prediction therefore depends on the positive scalar $\mathcal{R}_{\mathrm{EW}}$, not on an arbitrary split into vacuum-polarization, vertex, box, top, Higgs or QCD pieces. A future ultraviolet completion may calculate the same scalar from more primitive parameters; the prediction uses its measured electroweak value.

7. Six-shell closed-time-path matching action

7.1. Why the matching space has twelve real directions

The local centered-Gram shell is

$$\mathfrak{s} = \mathrm{Sym}^2(\mathbb{R}^3), \qquad \dim \mathfrak{s} = 6. \tag{96}$$

Its six coordinates comprise one trace direction and five traceless directions before relational reduction. A closed-time-path influence contains a forward and backward source,

$$\mathfrak{s}_{\mathrm{CTP}} = \mathfrak{s}_+ \oplus \mathfrak{s}_-, \qquad \dim \mathfrak{s}_{\mathrm{CTP}} = 12. \tag{97}$$

The six-component coframe source and the forward/backward histories required for causal response fix the doubled dimension to twelve.

Let $Z \in \mathrm{Sym}^+(6)$ be a positive branch transfer. The corresponding signed CTP Hessian is represented by

$$\mathbb{H}_{\mathrm{CTP}}(Z) = \begin{pmatrix} Z & 0 \\ 0 & -Z \end{pmatrix}. \tag{98}$$

Its determinant magnitude is

$$|\det \mathbb{H}_{\mathrm{CTP}}(Z)| = (\det Z)^2. \tag{99}$$

The signs encode the forward-minus-backward action; the magnitude supplies the positive normalization closure.

7.2. Determinant character from gluing

A scalar normalization attached to a finite transfer should be basis invariant and multiplicative under source-target composition. The following standard character statement makes that requirement precise.

Proposition 7.1 (Positive transfer character)**.** *Let $\chi : GL^+(n,\mathbb{R}) \to \mathbb{R}_{>0}$ be continuous, invariant under conjugation, multiplicative,*

$$\chi(AB) = \chi(A)\chi(B), \tag{100}$$

and normalized so that $\chi(e^{tI}) = e^{nt}$. Then

$$\boxed{\chi(A) = \det A.} \tag{101}$$

Proof. For $A = e^X$ in the identity component, continuity and multiplicativity imply $\log \chi(e^X)$ is an additive conjugation-invariant linear functional of X. Every such functional on $\mathfrak{gl}(n)$ is a multiple of $\operatorname{Tr} X$. The normalization fixes that multiple to one, giving $\chi(e^X) = e^{\operatorname{Tr} X} = \det e^X$. Every $A \in GL^+(n)$ has a real polar decomposition connected to the identity, so the result extends to the full domain. □

With unit character weight per shell direction, the determinant is the unique continuous multiplicative scalar of the positive transfer.

7.3. Determinant-constrained finite action

Definition 7.1 (Electroweak determinant closure)**.** The positive scalar character of the doubled coframe transfer is identified with the observable electroweak closure ratio,

$$|\det \mathbb{H}_{\mathrm{CTP}}(Z)| = \mathcal{R}_{\mathrm{EW}}, \qquad \text{equivalently} \qquad (\det Z)^2 = \mathcal{R}_{\mathrm{EW}}. \tag{102}$$

This matching law joins the charged-current normalization to the universal coframe source at one event; the determinant-character and least-history results below determine its unique isotropic realization.

For $Z \in \mathrm{Sym}^+(6)$ and a real multiplier Λ, the corresponding cross-sector contribution to the finite event action is

$$\boxed{\mathcal{I}_{\mathrm{match}}[Z, \Lambda] = \frac{1}{2} \operatorname{Tr}[(\log Z)^2] + \Lambda \left(2 \log \det Z - \log \mathcal{R}_{\mathrm{EW}}\right).} \tag{103}$$

The first term is the squared geodesic length from the identity in logarithmic process coordinates. The second enforces the electroweak determinant closure (102). An overall positive coefficient multiplying the history term rescales the action without changing its minimizer.

Theorem 7.2 (Least-history electroweak closure)**.** *For fixed $\mathcal{R}_{\mathrm{EW}} > 0$, the unique global minimizer of* (103) *on* $\mathrm{Sym}^+(6)$ *is*

$$\boxed{Z_* = \mathcal{R}_{\mathrm{EW}}^{1/12} I_6.} \tag{104}$$

Consequently, the universal shell matching factor is

$$\boxed{\mathcal{M}_{\mathrm{EW}}^{\mathrm{pred}} = \mathcal{R}_{\mathrm{EW}}^{1/12}.} \tag{105}$$

Proof. Let $x_1, \ldots, x_6$ be the eigenvalues of $\log Z$. The constraint is

$$2 \sum_{A=1}^{6} x_A = \log \mathcal{R}_{\mathrm{EW}}. \tag{106}$$

The history cost is $\frac{1}{2} \sum_A x_A^2$. At fixed sum,

$$\sum_A x_A^2 = 6\bar{x}^2 + \sum_A (x_A - \bar{x})^2 \geq 6\bar{x}^2, \tag{107}$$

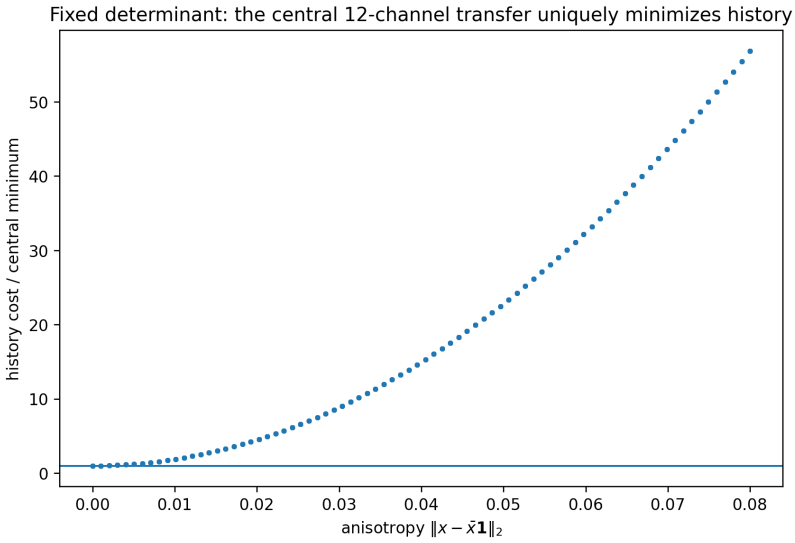


Figure 5: Least-history theorem. At fixed doubled determinant, every anisotropic redistribution of the six logarithmic eigenvalues increases the process-history cost. The central transfer is the unique minimum.

with equality only when every $x_A = \bar{x}$. Equation (106) gives

$$\bar{x} = \frac{\log \mathcal{R}_{\mathrm{EW}}}{12}, \tag{108}$$

hence (104). Strict convexity in the logarithmic eigenvalues gives uniqueness. □

7.4. Preservation of the gravitational quotient and the horizon sector

The minimizer (104) is central on the complete six-dimensional shell. Writing $z = \mathcal{R}_{\mathrm{EW}}^{1/12}$, one has $Z_* = zI_6$, so $Z_* \operatorname{im} G_{\boldsymbol{\kappa}} = \operatorname{im} G_{\boldsymbol{\kappa}}$ and $Z_* \ker Q_{\boldsymbol{\kappa}} = \ker Q_{\boldsymbol{\kappa}}$. It therefore descends to multiplication by z on the explicit quotient (34). The physical rank remains two and the plus/cross representatives are not split. Because the same central coefficient multiplies the canonical maps, the source-rigidity identity (48) is preserved.

The factor also contains no K dependence. The horizon equation

$$\mathcal{S}_K = 2\pi \mathcal{Z}_K \tag{109}$$

compares entropy with the horizontal response before electroweak matching. Multiplying the later universal Newton vertex by a K-independent central transfer does not move its roots. Hence

$$\boxed{K_* = 362 \quad \text{is retained.}} \tag{110}$$

8. Electroweak-completed Fermi–Newton theorem

For an event length a, define

$$\lambda_F(a) = \frac{G_F}{\sqrt{2}\,a^2}, \qquad \lambda_g(a) = \frac{G}{a^2}. \tag{111}$$

Definition 8.1 (Controlled-volume Fermi–coframe matching)**.** The channel-resolved charged-current vertex and the universal rank-one coframe-volume vertex are two reductions of the same primitive event coupling. Tracing the completely occupied three-slot channel register therefore gives

$$\lambda_{\mathrm{vol}}(a) = D_K^{-3}\lambda_F(a), \tag{112}$$

with the coefficient fixed by Theorems 5.4 and 5.5.

The central shell transfer (104) multiplies (112) by $\mathcal{M}_{\mathrm{EW}}^{\mathrm{pred}}$.

Theorem 8.1 (Electroweak Fermi–Newton closure)**.** *For the finite cell of Definition 2.1, supplemented by the matching laws in Definitions 7.1 and 8.1,*

$$\lambda_g(a) = D_K^{-3}\mathcal{R}_{\mathrm{EW}}^{1/12}\lambda_F(a). \tag{113}$$

Therefore

$$\boxed{G_{\mathrm{pred}}(K) = \frac{G_F}{\sqrt{2}\,D_K^3}\mathcal{R}_{\mathrm{EW}}^{1/12}.} \tag{114}$$

For $K_* = 362$,

$$\boxed{G_{\mathrm{pred}} = \frac{G_F}{\sqrt{2}\,(107232946821)^3}\left[\frac{\sqrt{2}\,G_F M_W^2(1 - M_W^2/M_Z^2)}{\pi\alpha(0)}\right]^{1/12}.} \tag{115}$$

No measured gravitational quantity appears on the right-hand side.

Proof. Insert (111) into (113). The common event factor a^{-2} cancels. The selected sector and electroweak factor are fixed by (63) and (105). □

The minimization and determinant algebra are exact consequences of the two matching laws. Their physical content is tested independently: electroweak measurements fix $\mathcal{R}_{mEW}$, horizon consistency fixes K_*, and gravitational measurements test the resulting value of G.

9. Numerical prediction and uncertainty

From (95),

$$\boxed{\mathcal{M}_{\mathrm{EW}}^{\mathrm{pred}} = 1.003095524456518.} \tag{116}$$

The leading filled-sea value remains

$$G_0 = \frac{G_F}{\sqrt{2}D_*^3} = 6.65424440085231 \times 10^{-11}\ \mathrm{m^3\,kg^{-1}\,s^{-2}}. \tag{117}$$

The electroweak-completed prediction is

$$G_{\mathrm{pred}} = 6.709376335636802 \times 10^{-39}\ \mathrm{GeV^{-2}}, \tag{118}$$

$$G_{\mathrm{pred}} = \boxed{6.674842777134797 \times 10^{-11}\ \mathrm{m^3\,kg^{-1}\,s^{-2}}}. \tag{119}$$

Propagating the independent input uncertainties gives

$$\boxed{G_{\mathrm{pred}} = 6.67484(28) \times 10^{-11}\ \mathrm{m^3\,kg^{-1}\,s^{-2}}.} \tag{120}$$

The uncertainty is dominated by M_W, followed by M_Z.

The 2022 CODATA value, used only after the prediction, is

$$G_{\mathrm{CODATA}} = 6.67430(15) \times 10^{-11}\ \mathrm{m^3\,kg^{-1}\,s^{-2}}. \tag{121}$$

The value is from the 2022 CODATA adjustment [30]. Thus

$$\frac{G_{\mathrm{pred}} - G_{\mathrm{CODATA}}}{G_{\mathrm{CODATA}}} = 8.13235 \times 10^{-5}, \tag{122}$$

and the difference is 1.72 combined standard deviations.

For comparison, the factor inferred from the CODATA central value is

$$\mathcal{M}_{\mathrm{EW}}^{(G)} = \frac{G_{\mathrm{CODATA}}}{G_0} = 1.003013955896348. \tag{123}$$

With propagated uncertainties,

$$\mathcal{M}_{\mathrm{EW}}^{\mathrm{pred}} = 1.0030955(42), \qquad \mathcal{M}_{\mathrm{EW}}^{(G)} = 1.0030140(23), \tag{124}$$

and the two differ by 1.72 standard deviations.

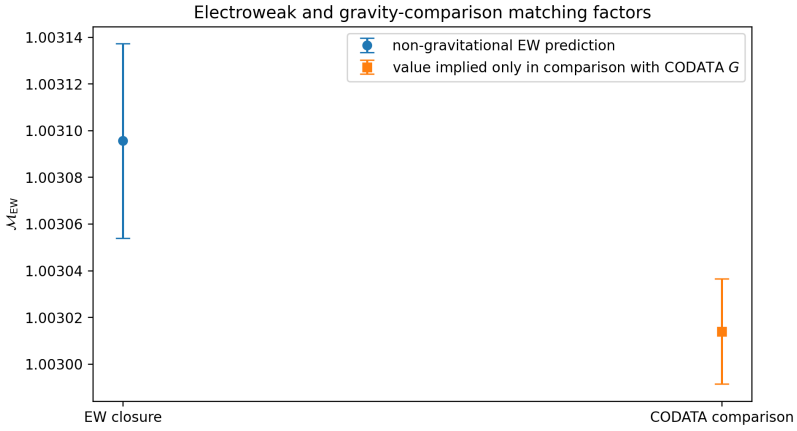


Figure 6: Electroweak matching factor and the factor inferred from the CODATA central value. Bands show propagated one-standard-deviation uncertainties.

9.1. Analytic uncertainty budget

Writing $r = M_W^2/M_Z^2$, logarithmic differentiation of (115) gives

$$\begin{aligned}
\frac{\partial \ln G}{\partial \ln G_F} &= \frac{13}{12}, \\
\frac{\partial \ln G}{\partial \ln \alpha^{-1}} &= \frac{1}{12}, \\
\frac{\partial \ln G}{\partial \ln M_W} &= \frac{1}{12}\left(2 - \frac{2r}{1-r}\right), \\
\frac{\partial \ln G}{\partial \ln M_Z} &= \frac{1}{12}\frac{2r}{1-r}.
\end{aligned} \tag{125}$$

At the central values these coefficients are 1.08333, 0.08333, -0.412922 and 0.579589, respectively. The relative uncertainty contributions are approximately 0.56, 0.000013, 39.6 and 12.7 parts per million.

9.2. The relation as a precision W-mass test

Because (115) is most sensitive to M_W, future W measurements directly test the closure. Current representative inputs from the PDG average, CMS, ATLAS, CDF II, and a recent Standard-Model fit give [25, 27, 28, 29, 23]:

Inverting the relation at the CODATA central value gives

$$M_W^{(G)} = 80.3783084 \text{ GeV}, \tag{126}$$

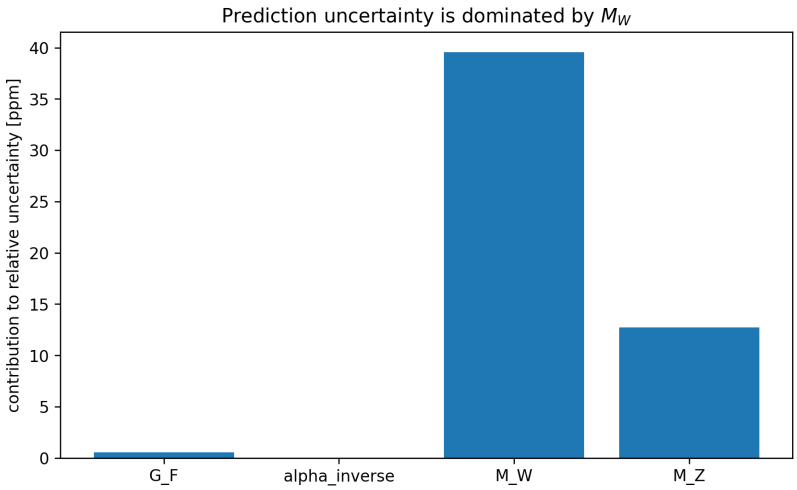


Figure 7: Uncertainty budget for G_{pred}. The present error is dominated by the direct W-mass average.

Table 2: Prediction obtained from representative W-mass inputs, with all other inputs fixed as in (94). Pulls are comparisons with CODATA and include the corresponding W uncertainty.

Input	M_W [GeV]	G_{pred} [10^{-11} SI]	pull
PDG 2026 average	80.3625(77)	6.674843	1.8σ
CMS	80.3602(99)	6.674922	1.7σ
ATLAS	80.3665(159)	6.674706	0.7σ
CDF II	80.4335(94)	6.672396	-5.3σ
2025 SM fit	80.3560(50)	6.675066	3.4σ

about 2.05 PDG-2026 standard deviations above the present average. This inversion displays the W-mass value at which the two central values coincide.

10. Origin of the twelfth root

The exponent in (105) follows from

$$6 \text{ centered-Gram shell directions} \times 2 \text{ closed-time-path branches} = 12. \quad (127)$$

The determinant constraint fixes the product of twelve signed-magnitude eigenvalues, while the least-history theorem assigns the same positive magnitude to each direction.

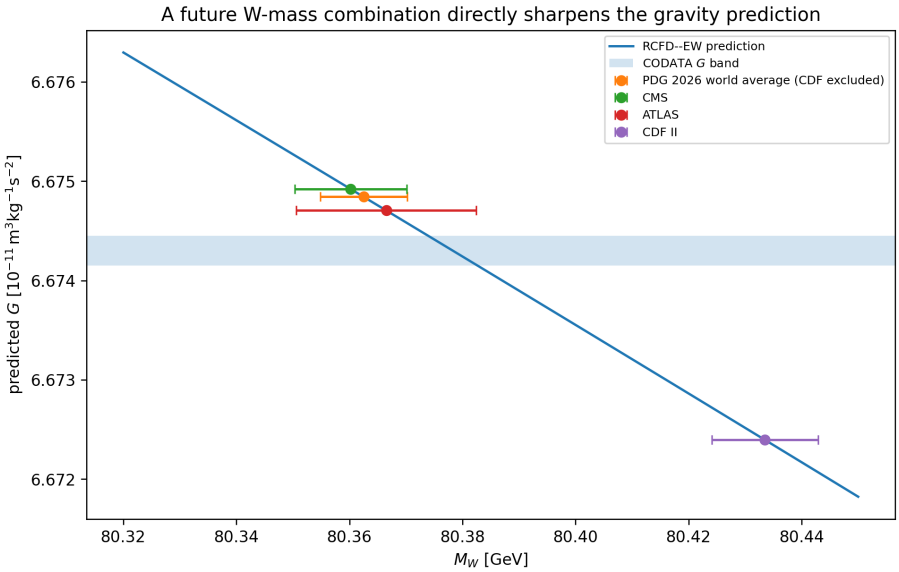


Figure 8: Predicted Newton constant as a function of the W-boson mass. The shaded band is the CODATA interval; markers show representative electroweak inputs.

To quantify sensitivity to an incorrect matching-space dimension, the executable also evaluates $\mathcal{R}_{\mathrm{EW}}^{1/n}$ for $n = 2, 3, 4, 5, 6, 8, 10, 12, 16, 20, 24, 32$. The model fixes $n = 12$ through (97); the alternatives show how rapidly the predicted value changes when the source space is altered.

The counterfactual dimensions confirm that the exponent is a structural input of the source space rather than a continuously adjustable coefficient.

11. Structural countermodels and robustness

Each load-bearing structural choice has a distinct countermodel.

Same-sea antisymmetric triple.. Replacing three ordered coframe slots by $\Lambda^3\mathcal{H}_K$ changes D^{-3} to $\binom{D}{3}^{-1} \sim 6D^{-3}$ and destroys the relation.

Undoubled shell.. Applying determinant closure to only one six-dimensional branch gives $\mathcal{R}_{\mathrm{EW}}^{1/6}$ and predicts G high by approximately 0.318%.

Physical quotient only.. Taking a root over the two on-shell tensor helicities gives $\mathcal{R}_{\mathrm{EW}}^{1/2}$ and predicts G high by about 1.57%. The matching action lives

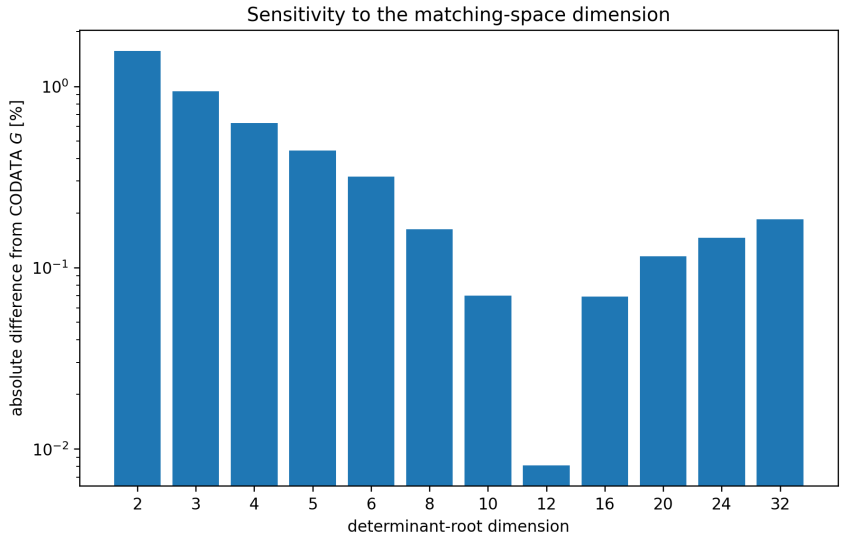


Figure 9: Sensitivity to the matching-space dimension. The vertical marker denotes the twelve-dimensional closed-time-path shell fixed by (97); the other bars are counterfactual source-space dimensions.

before relational reduction because source, constraint and noise normalizations are fixed on the complete shell.

Noncentral transfer.. An anisotropic Z with the same determinant always has larger history cost. More importantly, it would split shell directions and potentially the two tensor helicities. The least-history theorem excludes it.

Capacity-dependent matching.. A factor depending on K would feed back into the horizon equation and could move the selected sector. The electroweak scalar and central transfer are K independent; this independence is part of the model's falsifiable structure.

12. Horizon edge terms and the status of the sector theorem

The relation between conical entropy and the renormalized Newton coefficient can receive gauge-edge and contact contributions [7, 8]. In the present hybrid model the finite quantum Hilbert space contains occupied Julia channels, while the coframe and connection are collective sources. The sector equation therefore applies to the specified coframe-normal horizon algebra; quantizing additional edge sectors can modify it.

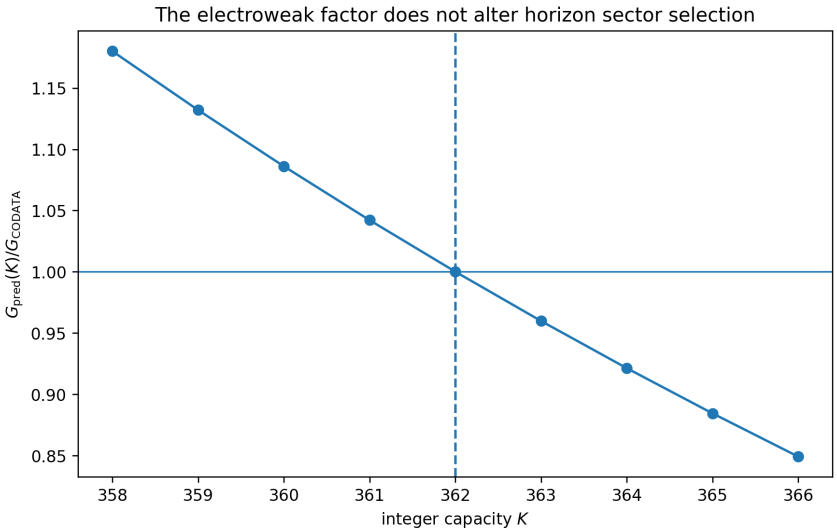


Figure 10: Integer-sector selectivity after electroweak completion. The matching factor is common to every sector, so the horizon-selected integer remains $K = 362$ and neighboring sectors stay several percent away.

A complete replica calculation must include all occupied electroweak edge modes, mediator contact terms, any quantized coframe or connection edge Hilbert space, the intrinsic Wald term, and finite-curvature coarea corrections. A shift of the high-capacity minimum away from 362 would change the numerical Newton prediction independently of the electroweak factor.

13. Conditional microscopic scales

The Fermi–Newton formula is independent of the equal-coefficient hybrid branch; the conversion to an event length uses that specialization. For

$$\widehat{G}_* \equiv \frac{\hbar G}{c^3 a^2} = 2.115621798636243 \times 10^{-12}, \tag{128}$$

the updated event scales are

$$a = 1.11124 \times 10^{-29}\ \mathrm{m}, \tag{129}$$
$$\tau = 3.70670 \times 10^{-38}\ \mathrm{s}, \tag{130}$$
$$a^{-1} = 1.77573 \times 10^{13}\ \mathrm{GeV}, \tag{131}$$
$$M_{\mathrm{rec}} = 1.77573 \times 10^{13}\ \mathrm{GeV}, \tag{132}$$

$$\hbar\Omega_{\mathrm{pair}} = 5.57188 \times 10^{13}\ \mathrm{GeV}. \tag{133}$$

These are the ultraviolet scales associated with the equal-coefficient branch.

The corresponding Planck masses obtained directly from (119) are

$$M_P = 1.2208405 \times 10^{19}\ \mathrm{GeV}, \qquad \overline{M}_P = 2.4352244 \times 10^{18}\ \mathrm{GeV}. \tag{134}$$

14. Relation to electroweak precision and induced gravity

The electroweak ratio (90) is familiar from precision Standard Model bookkeeping: in the G_F scheme, $\alpha_{G_F} = \alpha(0)(1 + \Delta r)$ [21, 22, 23]. The finite coframe transfer uses this observable closure through its doubled determinant character and distributes it by least history across twelve shell directions.

Sakharov induced gravity and species arguments relate gravitational stiffness to quantum matter response [1, 10]. The present construction differs in separating three operations: horizon entropy selects a discrete representation rank; complete occupation gives an invariant D^{-3} volume-channel reduction; electroweak determinant closure supplies a finite central transfer. None of these steps is a conventional one-loop species sum.

The model also differs from quantum cellular automata used only to reproduce free Weyl or Dirac kinematics [15, 16]. Here the route set is joined to a Gauss-projected coframe, an intrinsic geometric phase, relational constraints, a closed-time-path influence and a global horizon condition. This joined structure yields correlated tests in the horizon, electroweak, and gravitational sectors.

15. Tests and failure modes

The closure relation fails if any of the following occurs.

(F1) Complete horizon edge/contact accounting does not select $K = 362$.

(F2) The physical occupied state is not the complete lower branch, so the normalized channel state is not I_D/D.

(F3) The universal volume channel is not rank one on three ordered coframe slots.

(F4) The electroweak closure does not enter as the multiplicative determinant character of the doubled shell transfer.

(F5) The physically correct finite-history functional is not minimized by the logarithmic geodesic action (103).

(F6) The transfer is noncentral and splits the two tensor helicities or modifies the constraint algebra.

(F7) Future W and Z data move (115) outside the gravitational value beyond combined uncertainty.

(F8) Measured gravitational data are required anywhere in sector selection, determinant closure or parameter choice.

These alternatives cannot be absorbed by refitting a continuous coefficient. In particular, the CDF II W mass places the relation in substantial tension, while the present non-CDF average is compatible.

16. Discussion

The filled-sea relation $G_0 = G_F/(\sqrt{2}D_{362}^3)$ is approximately 0.30% below the CODATA central value and therefore requires a finite matching contribution. The determinant closure supplies that contribution from electroweak observables,

$$\mathcal{M}_{\mathrm{EW}} = \left(\frac{\alpha_{G_F}}{\alpha(0)}\right)^{1/12}, \tag{135}$$

so the gravitational comparison tests a coefficient fixed independently by G_F, M_W, M_Z, and $\alpha(0)$.

The central conceptual step is the separation between the determinant and its distribution. Exact gluing and basis invariance select the determinant as the scalar character. The electroweak closure fixes that determinant. The least-history action then selects its unique isotropic distribution. Neither the determinant root nor its exponent is adjusted to G.

The 1.72σ comparison is already a precision test rather than a scale fit: the formerly missing factor is fixed by electroweak observables and the model predicts how the result moves when M_W or M_Z changes. A different transfer character, horizon sector, or history functional produces a different numerical value and therefore directly falsifies the closure.

The relation shifts the experimental emphasis. The current uncertainty of the gravity prediction is not controlled by the torsion balance. It is controlled mainly by the W mass. A future electroweak combination can

therefore sharpen or reject a proposed quantum-gravity normalization without measuring gravity more precisely. The resulting cross-sector dependence makes the closure testable without direct access to the ultraviolet event scale.

17. Conclusion

The finite causal-cell construction ties the gravitational normalization to two independently determined structures. Generalized horizon entropy selects the capacity $K_* = 362$ and the occupied rank $D_{362} = 107232946821$; complete lower-branch occupation and the trilinear coframe-volume channel contribute D_{362}^{-3}. The doubled six-component coframe shell then fixes the remaining transfer through its determinant character and least logarithmic history,

$$\mathcal{M}_{\mathrm{EW}} = \left[\frac{\sqrt{2}\, G_F M_W^2 (1 - M_W^2/M_Z^2)}{\pi\alpha(0)}\right]^{1/12}. \tag{136}$$

Together they give

$$\boxed{G_{\mathrm{pred}} = 6.67484(28) \times 10^{-11}\ \mathrm{m^3\,kg^{-1}\,s^{-2}},} \tag{137}$$

using only G_F, $\alpha(0)$, M_W, and M_Z as dimensional and electroweak inputs. The result preserves the two-helicity quotient and the common tensor/source/static normalization.

The present uncertainty is dominated by M_W, so improved electroweak measurements sharpen the prediction directly. Complete horizon-edge accounting tests the capacity selection, while any noncentral transfer tests the helicity and constraint structure. The relation thus converts a microscopic gravity proposal into a linked set of quantitative checks across horizon thermodynamics, tensor propagation, static gravity, and precision electroweak physics.

Appendix A. Derivative equation for the selected recurrence margin

Differentiating (25) gives

$$0 = \sum_{J=0}^{K} d_J \frac{2(J+1)\xi_K}{(K+1)^2\sqrt{(1-\xi_K^2/(K+1)^2)\,(1+(J+1)^2\xi_K^2/(K+1)^2)}}$$

$$- 2d_K \frac{\mathrm{d}}{\mathrm{d}\xi} \left[m_K(\xi) \xi \sqrt{1-\xi^2} \right]_{\xi=\xi_K} . \tag{A.1}$$

The deterministic audit finds one root in $(0, 1/\sqrt{2})$ for every tested K and reproduces $\xi_K \to 0.6908100849582445\ldots$ at large K.

Appendix B. Direct replica formula

For a number-conserving Gaussian graph state with restricted correlation eigenvalues $(1+t_i)^{-1}$,

$$\operatorname{Tr} \rho_s^n = \prod_i \frac{1+t_i^n}{(1+t_i)^n}. \tag{B.1}$$

The capacity tower has $t_i = t_{J,K}$ repeated d_J times, giving (56). Differentiating $-\partial_n \ln \operatorname{Tr} \rho^n$ at $n=1$ gives (29).

Appendix C. Fock-space verification of the filled-sea theorem

For $D \le 6$, the executable constructs Jordan–Wigner matrices for every c_A and the filled state $|11\cdots1\rangle$. It verifies $\langle c_B^\dagger c_A \rangle = \delta_{AB}$ exactly in floating-point arithmetic. For random normalized vectors in $\mathbb{C}^{D^3}$ it verifies the rank-one trace D^{-3} below 2.8×10^{-17} and occupied-basis invariance below 1.7×10^{-16}.

Appendix D. Determinant character and least-history variation

For a positive matrix $Z = e^X$, every continuous multiplicative character is $e^{c \operatorname{Tr} X} = (\det Z)^c$. Unit weight per shell direction fixes $c = 1$. The CTP doubling gives $(\det Z)^2$.

Varying (103) in logarithmic coordinates $X = \log Z$ gives

$$\delta \mathcal{I}_{\mathrm{match}} = \operatorname{Tr}[(X + 2\Lambda I)\delta X]. \tag{D.1}$$

Thus $X = -2\Lambda I$. The constraint fixes $X = (\log \mathcal{R}_{\mathrm{EW}}) I/12$. Direct random fixed-determinant tests reproduce the determinant to 4.5×10^{-16} and find no lower anisotropic history cost.

Appendix E. Uncertainty propagation

Assuming independent inputs, (125) gives

$$\left(\frac{\sigma_G}{G}\right)^2 = \left(\frac{13}{12}\frac{\sigma_{G_F}}{G_F}\right)^2 + \left(\frac{1}{12}\frac{\sigma_{\alpha^{-1}}}{\alpha^{-1}}\right)^2 + \left[\frac{1}{12}\left(2 - \frac{2r}{1-r}\right)\frac{\sigma_{M_W}}{M_W}\right]^2 + \left[\frac{1}{12}\frac{2r}{1-r}\frac{\sigma_{M_Z}}{M_Z}\right]^2. \tag{E.1}$$

The result is $\sigma_G/G = 4.1560 \times 10^{-5}$. Correlations in a future combined electroweak fit should be propagated with its full covariance matrix rather than the independent-input approximation used here.

Appendix F. Unit conversion

In natural units G is in GeV^{-2}. The SI conversion is

$$G_{\mathrm{SI}} = G_{\mathrm{nat}}\frac{\hbar c^5}{(1\ \mathrm{GeV})^2}, \tag{F.1}$$

with $1\ \mathrm{GeV} = 1.602176634 \times 10^{-10}$ J. The conversion uses exact SI definitions and introduces no experimental uncertainty.

Appendix G. Reproducibility

The deterministic package:

(i) evaluates the finite recurrence, entropy and response sums and reproduces $K_* = 362$;

(ii) verifies the exact rank polynomial and high-precision selected data;

(iii) checks filled-sea and controlled-volume identities;

(iv) evaluates $\mathcal{R}_{\mathrm{EW}}$ and $\mathcal{R}_{\mathrm{EW}}^{1/12}$ from the declared inputs;

(v) verifies the doubled determinant and least-history minimum under random anisotropic deformations;

(vi) propagates the electroweak uncertainty analytically and numerically;

(vii) evaluates alternative determinant-root dimensions and representative W-mass scenarios;

(viii) regenerates every figure and records SHA-256 hashes.

Data and code availability

The source, deterministic verification program, machine-readable report, figures, and build instructions are supplied in the accompanying repository package.

Declaration of competing interest

The authors declare no competing financial interests or personal relationships that could have appeared to influence the work reported in this paper.

References

[1] A. D. Sakharov, Vacuum quantum fluctuations in curved space and the theory of gravitation, Sov. Phys. Dokl. **12** (1968) 1040.

[2] L. Susskind, J. Uglum, Black hole entropy in canonical quantum gravity and superstring theory, Phys. Rev. D **50** (1994) 2700, doi:10.1103/PhysRevD.50.2700.

[3] V. P. Frolov, D. V. Fursaev, Mechanism of generation of black hole entropy in Sakharov's induced gravity, Phys. Rev. D **56** (1997) 2212, doi:10.1103/PhysRevD.56.2212.

[4] R. M. Wald, Black hole entropy is the Noether charge, Phys. Rev. D **48** (1993) R3427, doi:10.1103/PhysRevD.48.R3427.

[5] E. Bianchi, Horizon entanglement entropy and universality of the graviton coupling, arXiv:1211.0522 [gr-qc].

[6] T. Jacobson, Entanglement equilibrium and the Einstein equation, Phys. Rev. Lett. **116** (2016) 201101, doi:10.1103/PhysRevLett.116.201101.

[7] S. N. Solodukhin, Newton constant, contact terms and entropy, Phys. Rev. D **91** (2015) 084028, doi:10.1103/PhysRevD.91.084028.

[8] A. Blommaert, S. Colin-Ellerin, Gravitons on the edge, J. High Energy Phys. **03** (2025) 116, doi:10.1007/JHEP03(2025)116.

[9] L. Freidel, E. R. Livine, The fine structure of $SU(2)$ intertwiners from $U(N)$ representations, J. Math. Phys. **51** (2010) 082502, doi:10.1063/1.3470931.

[10] G. Dvali, Black holes and large N species solution to the hierarchy problem, Fortschr. Phys. **58** (2010) 528, doi:10.1002/prop.201000009.

[11] R. Arnowitt, S. Deser, C. W. Misner, The dynamics of general relativity, Gen. Relativ. Gravit. **40** (2008) 1997, doi:10.1007/s10714-008-0661-1.

[12] B. S. DeWitt, Quantum theory of gravity. I. The canonical theory, Phys. Rev. **160** (1967) 1113, doi:10.1103/PhysRev.160.1113.

[13] J. W. York, Jr., Conformally invariant orthogonal decomposition of symmetric tensors on Riemannian manifolds and the initial-value problem of general relativity, J. Math. Phys. **14** (1973) 456, doi:10.1063/1.1666338.

[14] G. S. Joyce, Exact results for a body-centered cubic lattice Green's function with applications in lattice statistics. I, J. Math. Phys. **12** (1971) 1390, doi:10.1063/1.1665748.

[15] G. M. D'Ariano, P. Perinotti, Derivation of the Dirac equation from principles of information processing, Phys. Rev. A **90** (2014) 062106, doi:10.1103/PhysRevA.90.062106.

[16] A. Bisio, G. M. D'Ariano, P. Perinotti, Quantum walks, Weyl equation and the Lorentz group, Found. Phys. **47** (2017) 1065, doi:10.1007/s10701-017-0096-0.

[17] T. van Ritbergen, R. G. Stuart, Complete two-loop quantum electrodynamic contributions to the muon lifetime in the Fermi model, Phys. Rev. Lett. **82** (1999) 488, doi:10.1103/PhysRevLett.82.488.

[18] T. van Ritbergen, R. G. Stuart, On the precise determination of the Fermi coupling constant from the muon lifetime, Nucl. Phys. B **564** (2000) 343, doi:10.1016/S0550-3213(99)00572-6.

[19] A. Pak, A. Czarnecki, Mass effects in muon and semileptonic decays, Phys. Rev. Lett. **100** (2008) 241807, doi:10.1103/PhysRevLett.100.241807.

[20] V. Tishchenko et al. (MuLan Collaboration), Detailed report of the MuLan measurement of the positive muon lifetime and determination of the Fermi constant, Phys. Rev. D **87** (2013) 052003, doi:10.1103/PhysRevD.87.052003.

[21] A. Sirlin, Radiative corrections in the $SU(2)_L \times U(1)$ theory: a simple renormalization framework, Phys. Rev. D **22** (1980) 971, doi:10.1103/PhysRevD.22.971.

[22] J. Erler, A. Freitas, Electroweak model and constraints on new physics, in: Review of Particle Physics, Particle Data Group (2025 update), online review.

[23] G. Bozzi, L. Citelli, A. Vicini, Status of the W boson mass and the future of electroweak precision physics, arXiv:2506.01887 [hep-ph] (2025).

[24] F. Takahashi et al. (Particle Data Group), Review of Particle Physics, Int. J. Mod. Phys. A **41** (2026) 2630011.

[25] Particle Data Group, Gauge and Higgs bosons summary table: W mass, 2026 online listing.

[26] Particle Data Group, Z boson listing, 2026 online listing.

[27] CMS Collaboration, High-precision measurement of the W boson mass with the CMS experiment, Nature (2026), doi:10.1038/s41586-026-10168-5.

[28] ATLAS Collaboration, Measurement of the W-boson mass and width with the ATLAS detector using proton–proton collisions at $\sqrt{s} = 7$ TeV, Eur. Phys. J. C **84** (2024) 1309, doi:10.1140/epjc/s10052-024-13190-x.

[29] T. Aaltonen et al. (CDF Collaboration), High-precision measurement of the W boson mass with the CDF II detector, Science **376** (2022) 170–176, doi:10.1126/science.abk1781.

[30] P. J. Mohr, D. B. Newell, B. N. Taylor, E. Tiesinga, CODATA recommended values of the fundamental physical constants: 2022, Rev. Mod. Phys. **97** (2025) 025002, doi:10.1103/RevModPhys.97.025002.